Available online at www.sciencedirect.com

ScienceDirect

Geochimica et Cosmochimica Acta 75 (2011) 4951–4962

Geochimica et Cosmochimica Acta

www.elsevier.com/locate/gca

Siderite dissolution in the presence of chromate

Yuanzhi Tang, Scot T. Martin *

School of Engineering and Applied Sciences and Department of Earth and Planetary Sciences, Harvard University, Cambridge, MA 02138, USA

Received 30 July 2010; accepted in revised form 7 June 2011; available online 23 June 2011

Abstract

Siderite ($FeCO_3$) is an important reduced phase iron mineral and end product of bacteria anaerobic respiration. This study addresses its dissolution behavior in the presence of the oxidant chromate, which is a common environmental contaminant. Macroscopic dissolution experiments combined with microscopic observations by atomic force microscopy show that at $pH < 4.5$ the dissolution rate with chromate is slower than that in control solution without chromate. Isolated deep dissolution pits and clustered shallow pits occur simultaneously with surface precipitation. The implication is that the surface precipitate inhibits further dissolution. For $5 < pH < 9.5$, the slowest dissolution and the fastest precipitation rates are observed, both at edge steps and on terraces. For $pH > 10$, the dissolution rate in the presence of chromate exceeds that of the control, plausibly due to electron transfer facilitated by $\left[Fe^{3+}(OH)_4\right]^-$. Dissolution and re-precipitation of round hillocks are observed. X-ray photoelectron spectroscopy indicates the presence of Cr(III) as well as reaction products in a hydroxide form. Based on the redox reaction mechanism, macroscopic dissolution behavior, and previous studies on the reaction products of Fe(II) with Cr(VI), we propose the formation of a low solubility nano-sized Cr(III)–Fe(III)-hydroxide as the surface precipitate. Results from this study provide a basis for understanding and quantifying the interactions between reduced-iron minerals and aqueous-phase oxidants.

1. INTRODUCTION

Iron-containing minerals are key regulators in controlling the redox reactions and the energy flow between inorganic (e.g., redox sensitive metals) and organic components (e.g., microbes or molecular shuttles) in nature (Lovley, 1991; Nealson and Saffarini, 1994; Wielinga et al., 2001; Hansel et al., 2003). Among various reduced-phase iron minerals, siderite ($FeCO_3$) has wide occurrence in various environmental settings, such as marine deposits and terrestrial sedimentary rocks. Although the pE–pH range experienced by siderite in these natural settings is limited, siderite nonetheless plays an important role in the biogeochemical cycle of iron. Siderite is an important end product of bacterial anaerobic respiration in nature (Coleman et al., 1993) and in laboratory studies (Zachara et al., 1998; Liu et al., 2001). In aquatic environments, the seasonal change of pH and dissolved oxygen (La Force et al., 2002; Smedley and Kinniburgh, 2002) can cause the dissolution of siderite and the subsequent release of Fe(II), which can be converted to Fe(III) under oxidizing conditions and subsequently precipitate as iron (oxy)hydroxide minerals at intermediate to alkaline pH range. These iron (oxy)hydroxides generally have limited solubility and high surface area. They can be utilized by bacteria anaerobic respiration and thereby reduced to Fe(II). The hydroxides are also active scavengers of heavy metal and radionuclide contaminants through mechanisms of surface adsorption, precipitation, or incorporation, thereby affecting the fate and transport of these contaminants (Ahmed et al., 2004).

Many studies have addressed the formation, dissolution, and oxidation of siderite at the field scale (Stel, 2009) as well as its bulk precipitation and dissolution rate in low-temperature environments (Braun, 1991; Greenberg and Tomson, 1992; Jensen et al., 2002; Silva et al., 2002). The dissolution rate of siderite has also been studied at higher temperatures and pressures, as related to CO_2 sequestration and deep rock injection (Benezeth et al., 2009; Golubev et al., 2009;

---

* Corresponding author.
E-mail address: scot_martin@harvard.edu (S.T. Martin).

0016-7037/$ - see front matter © 2011 Elsevier Ltd. All rights reserved.
doi:10.1016/j.gca.2011.06.024

Testemale et al., 2009). Relatively few studies, however, have addressed the surface-controlled dissolution behavior of siderite under various environmental conditions (Van Cappellen et al., 1993; Pokrovsky and Schott, 2002; Duckworth and Martin, 2004a, b; Duckworth et al., 2004; Testemale et al., 2009). Duckworth and Martin (2004a, b) compared siderite dissolution behavior under anoxic and oxic conditions and found that the anoxic dissolution rate of siderite under various pH conditions followed parallel proton- and water hydrolysis-promoted dissolution pathways. In the presence of molecular oxygen, the dissolution rate between pH of 6.0 and 10.3 decreased below the limit of detection, as explained by the surface precipitation of ferrihydrite. For $pH > 10.3$, the oxic dissolution rate was greater than under the corresponding anoxic conditions, as was explained by rapid electron transfer between dissolved O_2 or $[Fe^{3+}(OH)_4]^-$ and surficial $>Fe^{II}$ hydroxyl groups. These results were a first step in providing a basis for understating siderite surface reactivity and redox reactions for the complex yet realistic variability of environmental conditions.

In this study, we examined the role of Cr(VI) in the surface-controlled dissolution behavior of siderite. We chose Cr(VI) because it is a strong oxidant and a significant anthropogenic metal contaminant (Palmer and Wittbrodt, 1991). Several studies have examined the use of siderite for Cr(VI) remediation through mechanisms of Cr(VI) reduction to Cr(III) by Fe(II), sorption of Cr(VI) and Cr(III) ions to the surface of siderite, and the precipitation of low solubility Cr(III)–Fe(III)-(oxy)hydroxides (Blowes et al., 1997; Erdem et al., 2004). These studies primarily focused on the remediation of Cr(VI) and did not address the dissolution behavior of siderite, which is the mechanistic requirement for understanding the redox and precipitation processes. Herein we use atomic force microscopy (AFM) equipped with a flow-through setup to measure simultaneously macroscopic and microscopic dissolution. Chemical and structural characteristics of the surface reaction products are examined ex situ using X-ray photoelectron spectroscopy (XPS).

2. EXPERIMENTAL

2.1. Mineral specimen and surface preparation

A siderite specimen (sample # 134827, Ivigtut, Greenland) was obtained from the Harvard University Mineralogical Museum. Yellowish to greenish translucent crystals of rhombohedral shapes were selected by visual inspection. Some of the selected crystals were finely ground for X-ray diffraction analysis on a Scintag XDS2000 diffractometer, which confirmed the siderite structure (PDF# 831764) and the absence of detectable impurity phases. The nominal detection limit for a well-crystallized material was 3%. Composition analysis of the same siderite specimen using proton-induced X-ray emission spectroscopy (PIXE) was previously reported as 95.35% Fe purity, with 4.47% Mn and trace amounts (<0.04%) of other species including Zn, Ca, and Sr (Duckworth and Martin, 2004b).

Before each set of dissolution experiments, a fresh siderite surface was prepared by cleaving a crystal along the $\{10\bar{1}4\}$ plane of perfect cleavage. The cleaved crystal was then attached to a steel puck using warmed dental modeling wax (Cavex, Holland), with the fresh surface facing up. The wax covered the edge of the sample so that only the top surface was exposed to the dissolution liquor. An optical image of the surface was recorded using a digital camera and the geometric surface area was calculated using Adobe Photoshop.

2.2. Preparation of dissolution liquor

The solutions used in this study were prepared with ACS grade reagents and deionized water (18 MΩ cm). K_2CrO_4 and $NaNO_3$ (Alfa Aesar) were dissolved to prepare a dissolution liquor of 1 mM K_2CrO_4 in 10 mM $NaNO_3$ background electrolyte, hereafter referred to as the Cr solution. Two sets of control solutions were prepared: deionized water and 10 mM $NaNO_3$ solution, referred to as control-water and control-$NaNO_3$, respectively. Before the start of each dissolution experiment, 200 mL of each of the three solutions was deoxygenated by purging overnight with water-saturated argon gas at a rate of 1 L min^{-1}. The pH values were adjusted between 1 and 11.5 using HCl (VWR) and NaOH (Acros) solutions. The prepared dissolution liquors were immediately drawn into 60 mL syringes and capped until use.

2.3. Speciation calculation

Aqueous speciation and saturation ratios with respect to solid phases at experimental conditions were calculated using the program PHREEQC Interactive (Parkhurst and Appelo, 1999). Saturation ratios of solid phases were quantified by the saturation index (SI), defined as $SI = \log(IAP/K_{eq})$, where IAP is the ion activity product and K_{eq} is the solubility product.

2.4. In situ atomic force microscope (AFM) flow-through experiments

A Nanoscope IIIa Multimode SPM (Digital Instruments) equipped with a fluid cell was used for in situ AFM image acquisition. In a typical experiment, the siderite surface that was cleaved and mounted on the steel puck was placed on the piezoelectric scanner, and a drop of deoxygenated deionized water was immediately placed on the sample surface, thereby obviating surface oxidation by O_2 from the air as well as the formation of bubbles. The fluid cell was immediately placed over the sample, and the control solution or Cr solution was introduced in continuous flow using a syringe pump through the cell at a rate of 0.2–0.7 mL min^{-1}. In a typical dissolution experiment with Cr solution, the surface was first cleaned using deoxygenated water to eliminate possible contaminants or debris remaining after cleavage. This process generally took 2–4 h, after which the Cr solution was introduced. Effluent from the fluid cell was monitored using a vertical-flow pH electrode (Cole Parmer) and was collected periodically into test tubes by a fraction collector (Teledyne Isco). The collected solution was immediately acidified using 5 μL of concentrated nitric acid and analyzed off-line for total iron concentration $[Fe]_T$ (nM) using an atomic absorption spectrometer equipped with a graphite furnace (AAS-GF; Perkin Elmer).

The siderite dissolution rate R ($mol\,m^{-2}\,s^{-1}$) of each experiment was calculated as:

$$R = [Fe]_T Q/A \tag{1}$$

for a flow rate Q ($L\,s^{-1}$) and a geometric surface area A (m^2) (Shiraki et al., 2000; Duckworth and Martin, 2003, 2004b). Dissolution rates obtained at different flow rates were self-consistent (variation <3.5%), suggesting that the overall dissolution was surface-controlled.

AFM images of the surface were collected in situ in contact mode using oxide-sharpened Si_3N_4 nanoprobes (Digital Instruments). Images were collected for areas of 1–100 μm^2 at scan rates of 1–3 Hz. Off-line image analysis followed standard procedures, including plane fitting, flattening, and height analysis using the programs WSxM v4.0 Develop 12.6 (Horcas et al., 2007) and Igor Pro 6.1 (WaveMetrics).

2.5. X-ray photoelectron spectroscopy (XPS) sample preparation and measurements

XPS data were collected on siderite surfaces that were reacted with Cr solutions at pH values of 2.8, 6.9, and 11.2 for varied time. After reaction, surfaces were gently washed with 1 mL deoxygenated deionized water at the end of AFM experiments to remove any solution residue, dried under a nitrogen gas, and analyzed ex situ by XPS. Several reference compounds were also analyzed, including a freshly cleaved and unreacted $FeCO_3$ surface, α-Fe_2O_3 (hematite), α-FeOOH (goethite), Cr_2O_3 (Acros Organics), and K_2CrO_4 (Alfa Aesar). Hematite (sample #138797, Brazil) was obtained from the Harvard University Mineralogical Museum. Goethite was synthesized following the methods of Schwertmann and Cornell (2000) and its structure confirmed by X-ray diffraction.

Chromium-reacted siderite crystals on the AFM pucks were fixed to the XPS sample stage using carbon tape. An aluminum foil, cut with a small opening to expose only the mineral surface, was placed around the crystal to increase conductivity. Unreacted siderite and hematite crystals were mounted directly on the sample stage with carbon tape, and a conductive path was made between the sample and stage with carbon paint. Powdered samples were pressed onto a carbon tape fixed to a stainless steel disc, and the exposed surface was pressed flat using a glass slide.

XPS analysis was conducted using an ESCA SSX-100 X-ray photoelectron spectrometer. The spectrometer was equipped with a monochromatized Al Kα X-ray source. The base pressure in the analytical chamber was 10^{-9} Torr. Spectra were collected at Fe 2s, Cr 2s, O 1s, and C 1s energies using a 600 μm spot size and a fixed pass-energy of 50 eV. Binding energies were corrected using the C 1s adventitious carbon peak (284.6 eV). Data processing used the program CasaXPS v2315.

3. RESULTS AND DISCUSSION

3.1. Macroscopic dissolution behavior

Fig. 1 shows representative time course profiles of pH and total iron concentration for the dissolution experiments. The pH value reaches steady state, both after the injection of the control solution and after switching to the Cr solution. After an initial transient at the beginning of each injection, total Fe concentration also obtains steady state. Initial transients have previously been observed for siderite and rhodochrosite (Duckworth and Martin, 2004a, b). They are possibly explained by the dissolution of high-energy sites created during cleavage or alternatively by the initial formation of deep pits at dislocations (Duckworth and Martin, 2003, 2004a).

Fig. 2A shows the dissolution rate of siderite for the two sets of controls in which no oxidant is present. The results of each follow similar trends. The dissolution rate is $\sim 10^{-8.6}\,mol\,m^{-2}\,s^{-1}$ for pH > 6 and gradually increases for more acidic pH, reaching $\sim 10^{-6}\,mol\,m^{-2}\,s^{-1}$ at pH = 2. The dissolution kinetics of divalent metal carbonates have been attributed to two parallel reactions occurring at the mineral–water interface: protonation of mineral surface at acidic pH and hydration of surface metal sites at neutral to alkaline pH (Plummer et al., 1978; Pokrovsky and Schott, 2002; Duckworth and Martin, 2004a, b; Testemale et al., 2009). For our experimental conditions, the calculated saturation index with respect to siderite is below 0, indicating that the system is far from equilibrium. In this case, the overall dissolution rate optimized to our data set can be expressed by a mechanistic model as:

$$R_{control} = 10^{-5.34}[H^+]^{0.61} + 10^{-8.61} \tag{2}$$

This model is shown as the solid line in Fig. 2A and B. Table 1 shows that the model parameters are in good agreement with those of previous studies conducted at similar experimental conditions.

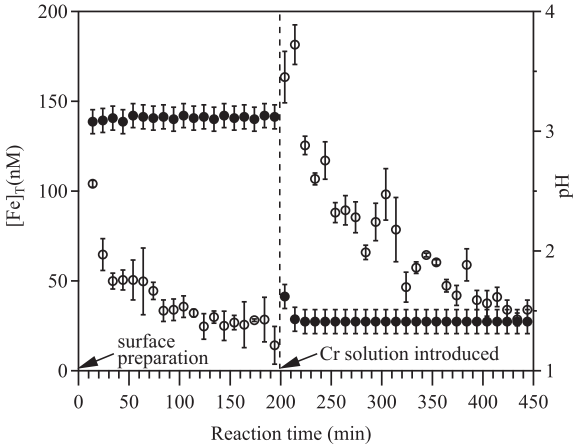

Fig. 1. Representative time series of total Fe concentration $[Fe]_T$ in the effluent (left axis) for step changes in pH (right axis). $[Fe]_T$ and pH are shown in open and closed circles, respectively.

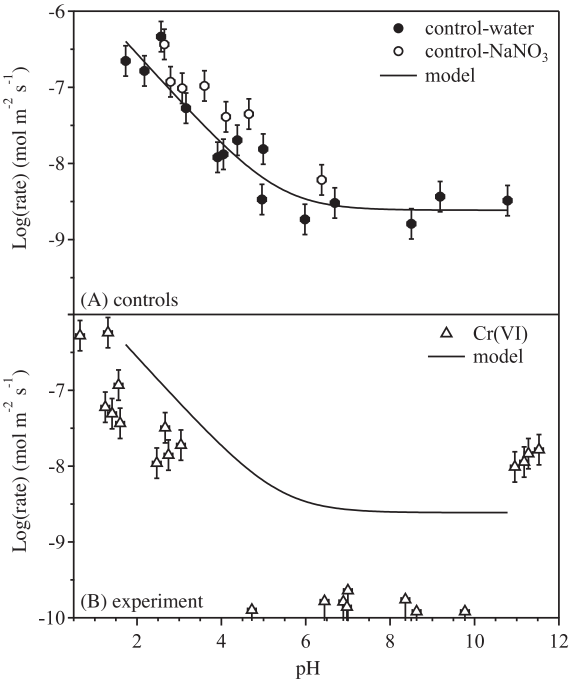

Fig. 2. Macroscopic dissolution rate of siderite as a function of pH for (A) controls of deionized water or 10 mM $NaNO_3$ solutions and (B) the experiment of 1 mM Cr(VI) as oxidant in 10 mM $NaNO_3$. The solid line is the mechanistic model calculated for the dissolution rate in control water (cf. Eq. (2)). The uncertainty bars that extend to the abscissa indicate lower limits based on the analytical detection limit of the experiments.

Fig. 2B shows the pH-dependent dissolution rate in the presence of the oxidant Cr(VI). For acidic pH ($pH < 4.5$), R_{Cr} is consistently lower than $R_{control}$. For example, at $pH = 2$ R_{Cr} is $\sim 10^{-7.5}$ mol m^{-2} s^{-1} and $R_{control}$ is $\sim 10^{-6}$ mol m^{-2} s^{-1}. For intermediate pH ($5 < pH < 9.5$), $[Fe]_T$ from the effluent is below the detection limit of GF-AAS. A lower limit of R_{Cr} is therefore established. For alkaline pH ($pH > 10$), R_{Cr} is significantly higher than the corresponding $R_{control}$. Specifically, at $pH = 11$ R_{Cr} is $\sim 10^{-7.9}$ mol m^{-2} s^{-1} compared to R_{Cr} of $\sim 10^{-8.6}$ mol m^{-2} s^{-1}.

The results using Cr(VI) as an oxidant can be compared to those reported by Duckworth and Martin (2004b) for dissolution with dissolved oxygen as an oxidant. In the presence of oxygen, the siderite dissolution rate at $pH < 5.5$ was the same as in anoxic conditions. This result differs from our study using Cr(VI) as an oxidant, showing smaller dissolution rates compared to the control solution. At pH values between 6 and 10.3, the dissolution rate of Duckworth and Martin (2004b) was below detection limit, in agreement with our results. For $pH > 10.3$, Duckworth and Martin (2004b) also observed rapid dissolution, approaching $10^{-7.5}$ mol m^{-2} s^{-1}, again similar to our observations ($\sim 10^{-7.9}$ mol m^{-2} s^{-1}) using Cr(VI) as the oxidant.

3.2. Microscopic observations

In the control solutions, the images collected during dissolution show widespread surface etching, edge step retreating, and isolated deep dissolution pits. Under circumneutral to alkaline pH conditions, pits typically distribute along lines. Most pits have the shape of inverted rhombohedral pyramids, reflecting the symmetry of siderite. Some are flat-bottomed, truncated pyramids (Fig. S1). The formation of these deep isolated pits can arise from the presence of surface reactive sites such as dislocations (Macinnis and Brantley, 1992; Duckworth and Martin, 2004a). Under acidic conditions, isolated dissolution pits also form but

Table 1
Summary of parameters for the mechanistic model used to describe proton- and water-hydrolysis-promoted siderite dissolution.

Log $k(H^+)$ (mol m^{-2} s^{-1})*	n*	Log $k(H_2O)$ (mol m^{-2} s^{-1})*	Siderite source	Experimental conditions				Ref.
				pH	Temp. (°C)	Solution	P_{CO2} (bar)	
−4.42	0.75		Powder	0–6				(a)
−4.60	0.75	−8.65	Single crystal	1.5–12	25			(b)
		−8.9	Powder	5–8	25	0.01 M NaCl		(c)
−3.75	0.75		Polycrystalline	2–4	25	0.1 M NaCl	Up to 50	(d)
−2.20	0.96				60			
	0.94				80			
−1.42	0.90				100			
−4.35	1		Single crystal ($(Fe_{0.87}Mg_{0.12}Ca_{0.01})CO_3$)	1.1–1.6	50	0.1 M HCl	300	(e)
−3.40	1			1.1–2.5	75			
−2.77	1			1.1–4	100			
−5.34	0.61	−8.61	Single crystal		25	0.01 M $NaNO_3$		This study

(a) Dresel et al. (1989) as cited by Duckworth and Martin (2004b).
(b) Duckworth and Martin (2004b).
(c) Pokrovsky and Schott (2002).
(d) Golubev et al. (2009).
(e) Testemale et al. (2009).
* Rate constants and order of reaction as defined in mechanistic dissolution model $R = k(H^+)[H^+]^n + k(H_2O)$ (Pokrovsky and Schott, 2002; Duckworth and Martin, 2004a, b.)

in this case generally show an elongated feature (Fig. S1A). Clustered small shallow dissolution pits are also present at fine scale. Previous studies have attributed the formation of these shallow pits to the presence of clustered point defects (Macinnis and Brantley, 1992; Duckworth and Martin, 2004a). These observations are consistent with the previously reported pit morphologies of siderite under anoxic conditions (Duckworth and Martin, 2004a). In the presence of Cr(VI), no significant modification to the pit morphologies was observed. However, a new feature of simultaneous precipitation was observed, which was more pronounced for acidic and circumneutral conditions. In the following paragraphs we show representative images collected for acidic (Figs. 3–5), circumneutral (Fig. 6), and alkaline (Fig. 7) conditions.

The time series of images in Fig. 3 shows the development of clustered shallow pits as well as a precipitating surface overlayer in the presence of Cr solution at pH = 3. Fig. 3A–C shows that the pits on the left and lower side of the images (i.e., area outside of the black ellipse) coalesce into larger rhombohedral shaped pits. The histograms reveal that the pit depth gradually increases from 0.4 to 3.2 nm during this process. At the same time, small pits are filled by surface precipitates. After 60 min (image not shown), all pits disappear, primarily by filling.

In addition to widespread shallow pits at fine scale, development of isolated deep pits is also observed. Fig. 4 shows the evolution of a representative isolated deep pit after switching from the control solution (pH = 2.6) to the Cr solution (pH = 2.8). The height profiles in Fig. 4E indicate that the pit has an unchanged depth of ~20 nm after switching to Cr solution for 45 min but widens to the right side. After 111 min, the pit also widens to the left, with a hillock-shaped precipitate filling the right side. This precipitate is ~200 nm in diameter and ~12 nm higher than the surface. After 167 min, no further widening of the pit is observed. The precipitate grows to ~26 nm above the surface. In these images, widespread surface etching around the pit is also evident. With extended reaction time, the surface precipitate gradually builds up. Fig. 5 shows the deflection-mode image and height profile of a siderite surface after exposure to a Cr solution of pH = 3 for 23.3 h. Rounded hillock precipitates are apparent across the surface, with no preferential distribution to terrace or steps. The vertical heights of these precipitates are ~10 nm, with lateral diameters varying between 200 and 1000 nm.

Fig. 6 shows a set of representative images collected at circumneutral pH in the Cr solution. After the inlet is switched from the control to the Cr solution, the surface is rapidly covered by a film of precipitates. The height profile in Fig. 6B shows that the height of these precipitates is from 0 to 2 nm. Some of the larger precipitates grow as rounded hillocks, with sizes ranging from 2 to 3 nm. These precipitates, especially the less developed small ones, are loosely attached at the initial stage and can be removed by scanning the AFM tip at large contact force. Again, no preferential locations are observed for these precipitates; they appear both at edge steps and terraces on the surface.

At alkaline pH, surface morphology is dominated by dissolution, although simultaneous precipitation and reorganization of surface features are also sometimes observed. Fig. 7 shows the evolution of a siderite surface after exposure to Cr solution of pH = 11.5 for up to ~4 h. Surface feature *a* gradually dissolves and reorganizes from an irregular shape to a rounded shape. After 222 min, precipitates form on top of it, increasing the height from ~40 to

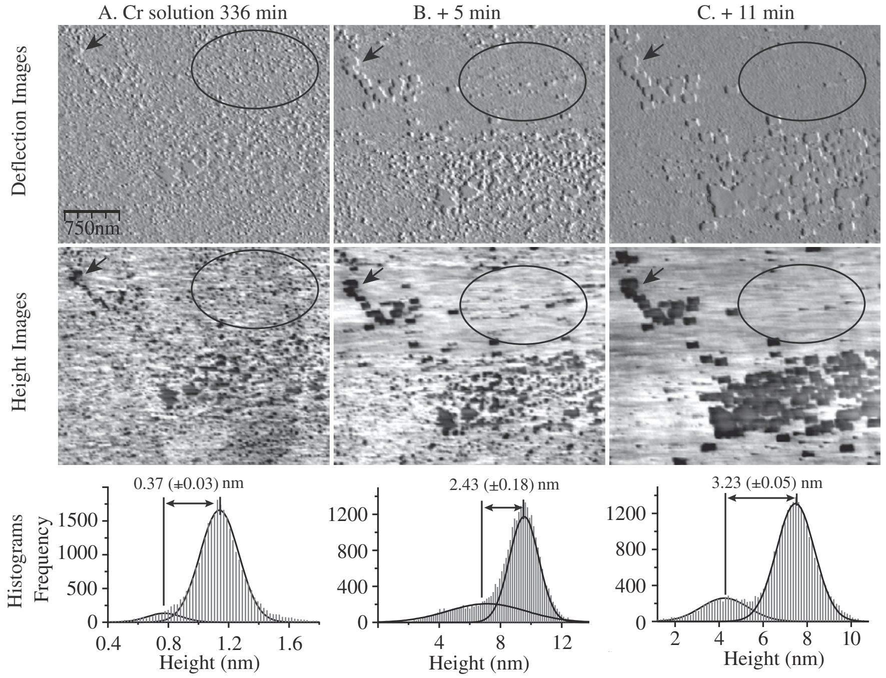

Fig. 3. AFM micrographs illustrating dissolution and precipitation over time on the surface of siderite when exposed to the Cr(VI) oxidant solution at pH 3. The black ellipse in each image highlights areas that are evident of precipitation. Outside the ellipse, dissolution is more evident in the series of images. The arrow serves as a point of reference referred to in the text.

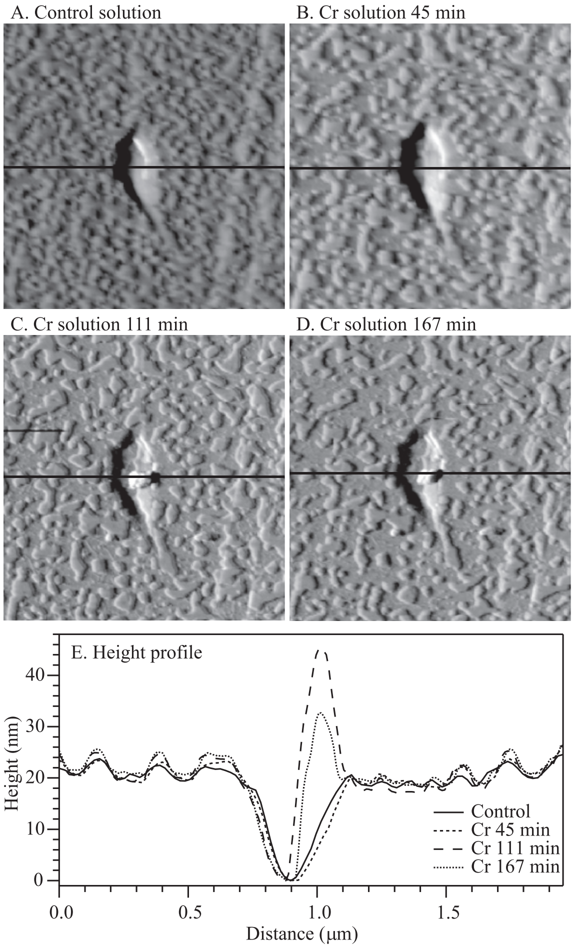

Fig. 4. AFM deflection-mode image showing (A) a representative dissolution pit in control solution (pH 2.6); (B–D) evolution of this pit after switching to Cr solution (pH 2.8) for 45, 111, and 167 min, respectivety; and (E) the corresponding height profiles on panels A–D.

~70 nm (Fig. 7F). At the same time, round hillocks such as features *b* and *c* gradually dissolve and decrease in size.

3.3. XPS analysis

XPS survey spectra as well as high-resolution Cr 2p, Fe 2p, and O 1s spectra were collected to provide chemical composition, oxidation state, and structure information. Survey spectra collected for siderite samples that had been reacted with Cr show the presence of Cr on the surface. XPS analysis is sensitive to the topmost 1–10 nm of an examined surface; therefore, the presence of Cr suggests the partitioning of Cr either as a surface-sorbed species or a surface precipitate. Previous studies indicate that Cr(VI) sorbs to mineral surfaces predominantly as an outer-sphere complex (Zachara et al., 2004) or a weak inner-sphere complex (Fendorf et al., 1997). By washing, these species are readily removed, therefore we do not expect a significant amount of surface-sorbed species as the source of the XPS signal intensity.

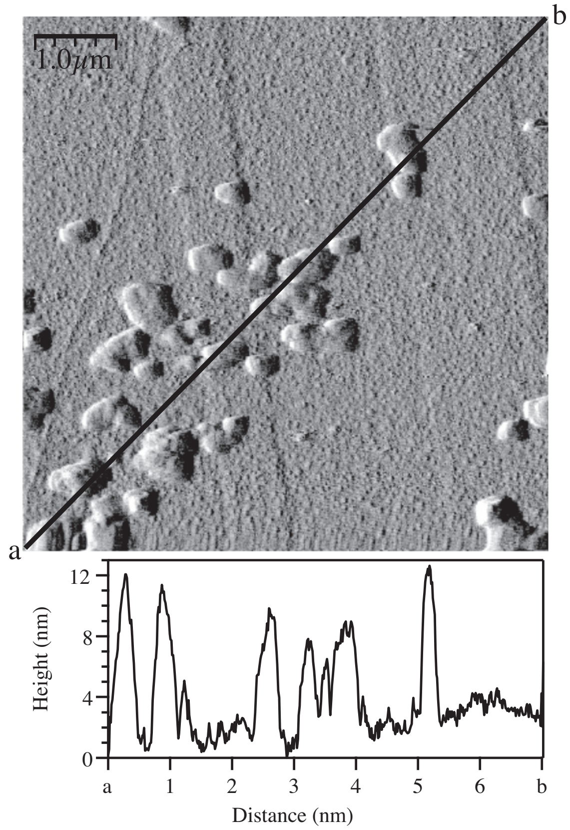

Fig. 5. (Top) AFM deflection-mode image and (bottom) height profile of the cross section from point *a* to *b* for a siderite surface after exposure to Cr solution at pH 3 for 23.3 h.

Cr 2p XPS spectra of K_2CrO_4, Cr_2O_3, and Cr-reacted siderite are presented in Fig. 8. Binding energies (BE) are indicated in the figure. The BEs of Cr(VI) as K_2CrO_4 correspond to Cr $2p_{3/2}$ at 578.9, $2p_{1/2}$ at 588.3, $2p_{3/2}$ satellite at 576.4, and $2p_{1/2}$ satellite at 587.3 eV.

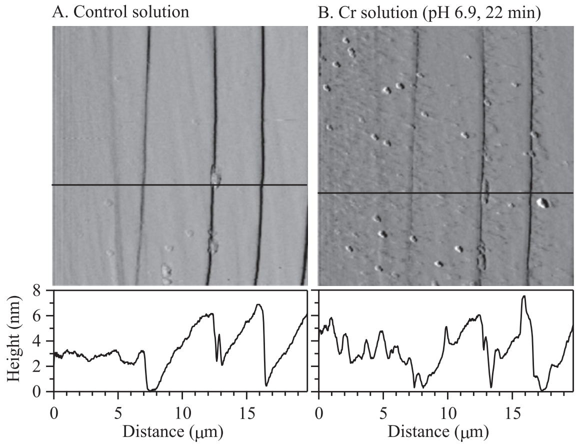

Fig. 6. AFM deflection image of (A) a siderite surface exposed in control solution at pH 2.6 for 221 min and (B) the same area after exposure to 1 mM Cr(VI) solution at pH 6.9 for 22 min.

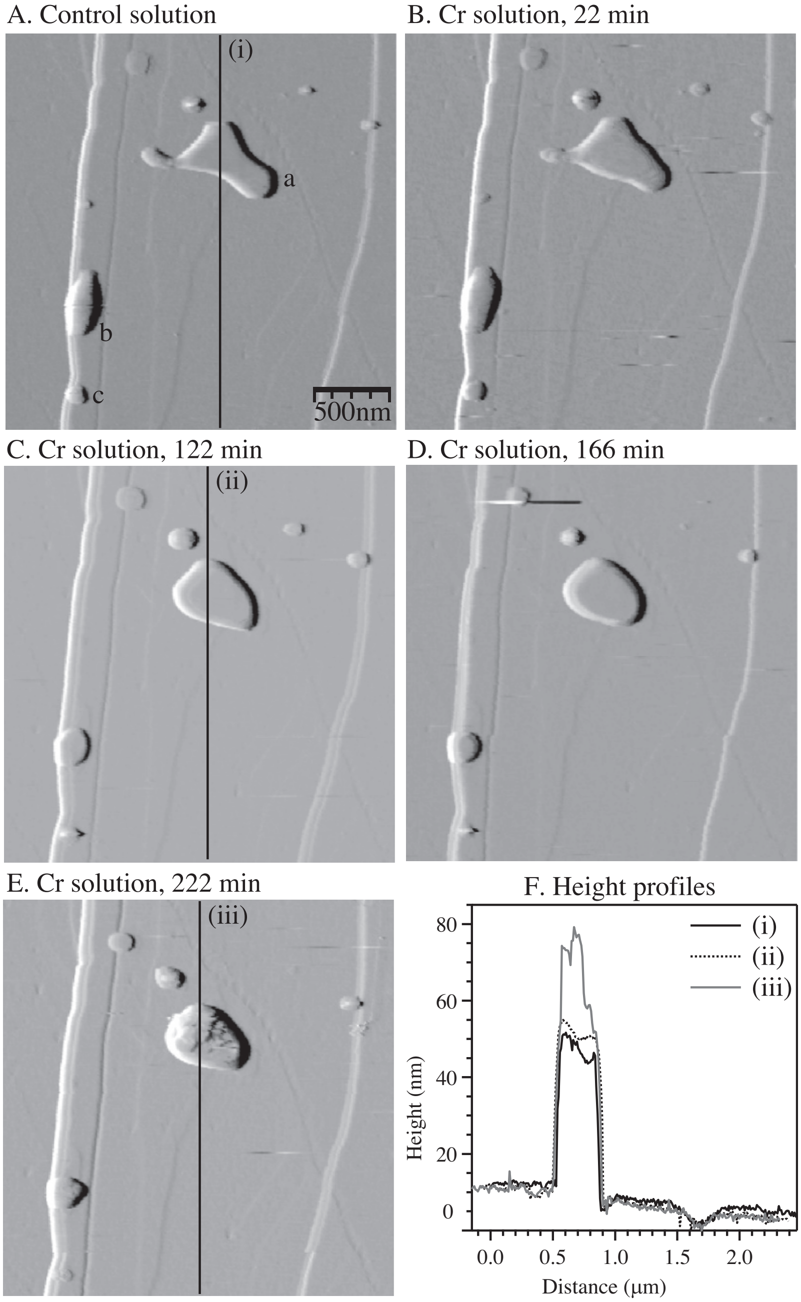

Fig. 7. AFM deflection images showing the evolution of siderite in (A) control solution (pH 2.4) and (B–E) after switching to Cr solution of pH 11.5 for 22, 122, 166, and 222 min, respectively. Panel (F) shows the height profiles of surface feature *a* across panels A, C, and E.

These values are in agreement with previously reported values of Cr $2p_{3/2}$ at 579.3 and $2p_{1/2}$ at 588.5 eV, with a separation of 9.1–9.2 eV (Stipp and Hochella, 1991; Sosulnikov and Teterin, 1992; Aronniemi et al., 2005). Cr_2O_3 lacks the two satellite peaks and has BEs of $2p_{3/2}$ at 576.4 and $2p_{1/2}$ at 586.3 eV, significantly lower than those of Cr(VI) and in agreement with previous studies (Aronniemi et al., 2005). The two Cr-reacted samples reacted at $pH < 10$ for 20 h have BEs at 576.8–576.9 eV and 586.3–596.8 eV for $2p_{3/2}$ and $2p_{1/2}$ peaks, respectively, similar to those of Cr(III) and significantly lower than those of Cr(VI), indicating that the Cr is retained on the siderite surface as Cr(III). Additional samples that are reacted at similar pH but shorter time (<4 h) also show peak positions that are indicative of the presence of Cr(III). Cr XPS spectra were also collected on five samples reacted with Cr(VI) at $pH > 10$. Two of the samples exposed to Cr(VI) to less than 4 hr show Cr 2p peaks, although noisy, with positions similar to that of Cr(III) (data not shown). Interestingly, no Cr signals were observed on the three crystals that are reacted for extended time (20 h). An attempt to resolve the Fe oxidation state from Fe 2p spectra was not successful due to a large interference from the underlying $FeCO_3$ substrate.

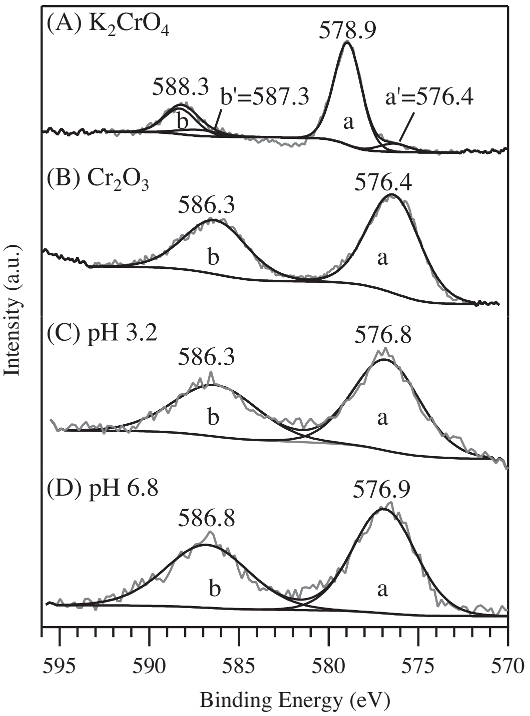

Fig. 8. High-resolution Cr 2p XPS spectra of (A) K_2CrO_4, (B) Cr_2O_3, and (C–D) siderite samples that were reacted with Cr(VI) solution at pH 2.8 and 6.9, respectively. Raw and fitted data are shown in gray and black lines, respectively. The Cr $2p_{3/2}$, $2p_{3/2}$ satellite, $2p_{1/2}$, and $2p_{1/2}$ satellite peaks are labeled as a, a′, b, and b′, respectively. Binding energies (eV) determined from peak positions are labeled next to each peak.

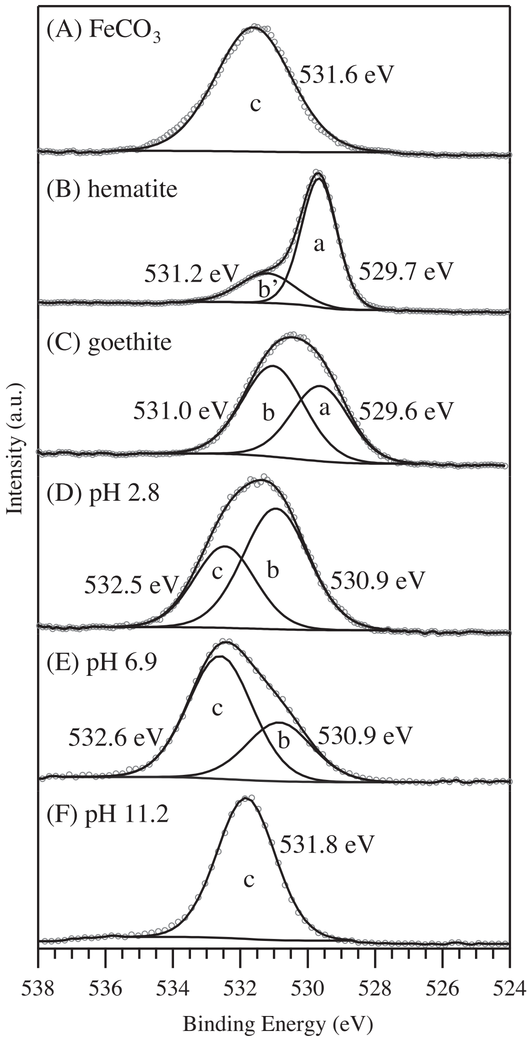

Fig. 9. High-resolution O 1s XPS spectra of (A) unreacted siderite, (B) hematite, (C) goethite, and (D)–(F) Cr-reacted siderite sample at pH 2.8, 6.9, and 11.2, respectively. Raw and fitted data are shown in open circles and black lines, respectively. The O 1s peak as in O^{2-}, OH^-, adventitious water/OH^-, and CO_3^{2-} are labeled as a, b, b′, and c, respectively. Binding energies (eV) determined from peak positions are labeled next to each peak.

O 1s XPS spectra were collected for known reference compounds to determine characteristic peaks for oxygen speciated as O^{2-}, OH^-, and CO_3^{2-}. The O 1s spectra and BEs are shown in Fig. 9. The spectrum collected for unreacted $FeCO_3$ has a major peak centered at 531.6 eV, similar to that reported for oxygen in CO_3^{2-}, e.g., $BaCO_3$ at 531.2 eV, $CaCO_3$ at 531.6–531.9 eV, $MnCO_3$ at 532.2 eV, and $FeCO_3$ at 532.3 eV (Stipp and Hochella, 1991; Sosulnikov and Teterin, 1992; Duckworth and Martin, 2004b). The FWHM of this peak (2.7 eV) is similar to the values of $FeCO_3$ reported by Duckworth and Martin (2004b), but slightly higher than reported values of other carbonate minerals, e.g., ~2.0 eV for $BaCO_3$ and $CaCO_3$ (Sosulnikov and Teterin, 1992). However, fitting the peak with multiple components did not improve the result. It is possible that the sample surface is slightly oxidized during the short exposure to atmosphere before putting into the XPS sample chamber. Hematite has a major peak centered at 529.7 eV, consistent with previously reported values of 529.8–530.2 eV for oxygen in O^{2-} (Junta Rosso and Hochella, 1996; Duckworth and Martin, 2004b; Spiccia and Casey, 2007). A minor shoulder at 531.2 eV is also present, likely due to the contribution from adventitious dissociated H_2O (Junta Rosso and Hochella, 1996). Goethite shows a broad peak with FWHM of 3.0 eV, which can be deconvoluted into two peaks: an O^{2-} peak at 529.6 eV and an OH^- peak at 531.0 eV. The BEs and separation values of these two peaks (1.4 eV) agree with literature values for O^{2-} (529.8–530.2 eV) and OH^- (531.0–531.9 eV), with a separation value of 1.1–1.9 eV (Duckworth and Martin, 2004b; Spiccia and Casey, 2007).

O 1s spectra were also recorded for the Cr-reacted siderite surfaces. The peaks for samples reacted at pH of 2.8 and 6.9 are broad (FWHM both at 3.1) and asymmetric. They can be deconvoluted into two peaks: (1) a peak at 530.9 eV that corresponds to the oxygen in OH^-, suggesting that the surface precipitate is a hydroxide; and (2) a peak at 532.5–532.6 eV that we assign as CO_3^{2-} peak. The CO_3^{2-} peak arises from the contribution of the underlying $FeCO_3$ substrate. Position of this peak is slightly higher than that observed value for the unreacted siderite reference (531.6 eV). For the siderite sample reacted at $\text{pH} = 11.2$, the spectra show a dominant peak centered at 531.8 eV, which is assigned to oxygen in CO_3^{2-}.

3.4. Reaction products in the presence of Cr(VI)

Duckworth and Martin (2004b) showed that in the presence of dissolved oxygen, Fe(II) released from siderite dissolution is oxidized to Fe(III) and precipitates as Fe hydroxide (ferrihydrite) for the pH range of 6–10.3. For pH <5, ferrihydrite precipitation is not thermodynamically favorable, and the macroscopic dissolution rate of Duckworth and Martin (2004b) is therefore similar to anoxic conditions. This result is much different from our results obtained using Cr(VI) as an oxidant. The macroscopic dissolution rate in Cr solution is almost an order of magnitude lower than that in the control solution. As a check, our control conditions are similar to those of Duckworth and Martin (2004b). We also observe precipitation for acidic pH (<5). The combination of this observation with that of a reduced dissolution rate indicates that the surface precipitates formed in the presence of Cr(VI) are different from the ferrihydrite formed under oxygen conditions. In particular, this new precipitate is much less soluble under acidic pH conditions.

From our XPS analysis, although we are not able to directly resolve Fe(III) species from Fe 2p spectra due to large interferences from the underlying $FeCO_3$ substrate, the presence of the Cr(III) species strongly points to a redox reaction between Fe(II) and Cr(VI) that results in Cr(III) and Fe(III) species. Combining these results with the O 1s observation showing the presence of a hydroxide species on the surface leads to the conclusion that the surface precipitate is either (1) a mixed Cr(III)–Fe(III)-hydroxide phase or (2) a discrete single solid assemblage of mixed Fe(III)-hydroxide and Cr(III)-hydroxide phases.

Many studies have shown that the reduction of Cr(VI) by Fe(II) and S^{2-} results in insoluble $Cr_{1-x}Fe_x(OH)_3 \cdot nH_2O$ phase (Sass and Rai, 1987; Patterson et al., 1997). Eary and Rai (1988) and Palmer and Wittbrodt (1991) report the rapid redox reaction:

$$\mathrm{Cr(VI)_{(aq)}} + 3\mathrm{Fe(II)_{(aq)}} \rightarrow \mathrm{Cr(III)_{(aq)}} + 3\mathrm{Fe(III)_{(aq)}} \tag{3}$$

The resulting Cr(III) and Fe(III) can hydrolyze, combine, and precipitate as a solid solution in slightly acidic to alkaline conditions:

$$x\mathrm{Cr(III)_{(aq)}} + (1-x)\mathrm{Fe(III)_{(aq)}} + (3+n)\mathrm{H_2O} \rightarrow \mathrm{Cr}_x\mathrm{Fe}_{1-x}\mathrm{(OH)}_{3(s)} \cdot n\mathrm{H_2O} + 3\mathrm{H}^+ \tag{4}$$

for which the Fe:Cr ratio is consistently measured as approximately 3.0 (i.e., $x = 0.25$), as one would expect from the stoichiometry of reaction 3. Solubility and structure studies have also suggested that the Cr(III)–Fe(III)-hydroxide phase is stable during the fast precipitation of Cr(III) and Fe(III) aqueous ions (Sass and Rai, 1987; Vajpei et al., 1989; Amonette and Rai, 1990; Tang et al., 2010). We are not aware of any study reporting separate Cr(III)- and Fe(III)-hydroxide phases during the redox reaction between Cr(VI) and Fe(II) or the co-precipitation of Cr(III) and Fe(III). Therefore, we assign the precipitates as nanocrystalline particles with a likely composition of $Cr_{0.25}Fe_{0.75}(OH)_3 \cdot nH_2O$. In agreement with the size dimensions, Tang et al. (2010) showed that the $Cr_xFe_{1-x}(OH)_{3(s)} \cdot nH_2O$ series has particles sizes of 1–2 nm. Although Schwertmann et al. (1989) and Amonette and Rai (1990) report the transformation of the initial nanocrystalline Cr–Fe-hydroxide phase into crystalline goethite with extended aging time (100 days) at high pH or temperature, for our experimental conditions at room temperature and with a reaction time shorter than 24 h we do not expect and did not observe such structural transformation.

3.5. Reaction mechanisms in the presence of Cr(VI)

A schematic presentation of the proposed reaction mechanisms for the Cr-initiated oxidation of the siderite surface, including surface precipitation, is shown in Fig. 10 for three different pH regimes. The mechanism includes the following aspects (A–C):

(A) The dissolution of siderite via parallel protonation and water hydrolysis reactions (cf. Section 3.1):

$$\mathrm{FeCO_{3(s)}} + \mathrm{H}^+ \rightarrow \mathrm{Fe}^{2+} + \mathrm{HCO_3^-} \tag{5}$$

$$\mathrm{FeCO_{3(s)}} + \mathrm{H_2O} \rightarrow \mathrm{Fe}^{2+} + \mathrm{HCO_3^-} + \mathrm{OH}^- \tag{6}$$

(B) A redox reaction between Cr(VI) and Fe(II). The speciation calculation of the Cr(VI) influent (Cr(VI) = 1 mM, $NaNO_3 = 0.01$ M, and $P_{O2} = 0$ atm) indicates that below pH of 5 $HCrO_4^-$ dominates (>95%) with less than 5% $Cr_2O_7^{2-}$. For increasing pH, the relative percentage of

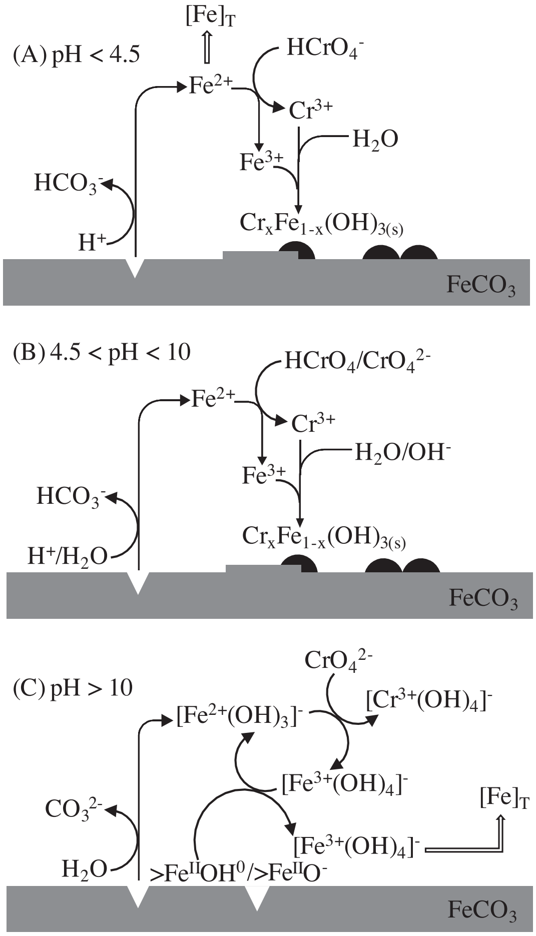

Fig. 10. Illustration of the proposed reaction mechanisms for the Cr-initiated oxidation of the siderite surface, including surface precipitation, for three different pH regimes.

$HCrO_4^-$ decreases and CrO_4^{2-} becomes more important. $HCrO_4^-$ and CrO_4^{2-} have equal abundance at $pH = 6.5$. CrO_4^{2-} dominates the Cr(VI) speciation for $pH > 8$. Previous studies show that the reduction of Cr(VI) by Fe(II)-bearing minerals such as biotite and Fe(II)-containing natural hematite only occurs in solutions in which dissolved Fe(II) exists (i.e., homogeneous reaction) instead of occurring directly at the mineral surface (i.e., heterogeneous reaction) (Eary and Rai, 1989). The rate of Cr(VI) reduction and Fe(II) oxidation thus depends on the rate of mineral dissolution. Therefore, depending on the pH, the redox reaction between Fe(II) and Cr(VI) can be written as:

$$3Fe^{2+} + HCrO_4^- + 7H^+ \rightarrow 3Fe^{3+}_{(aq)} + Cr^{3+}_{(aq)} + 4H_2O \qquad (7)$$

$$3Fe^{2+} + CrO_4^{2-} + 8H^+ \rightarrow 3Fe^{3+}_{(aq)} + Cr^{3+}_{(aq)} + 4H_2O \qquad (8)$$

(C) The precipitation of Cr(III)–Fe(III)-hydroxide phase (cf. Section 3.4):

$$Cr^{3+}_{(aq)} + 3Fe^{3+}_{(aq)} + 12H_2O \rightarrow 4Cr_{0.25}Fe_{0.75}(OH)_{3(s)} + 12H^+ \qquad (9)$$

$$Cr^{3+}_{(aq)} + 3Fe^{3+}_{(aq)} + 12OH^- \rightarrow 4cr_{0.25}Fe_{0.75}(OH)_{3(s)} \qquad (10)$$

The macroscopic, microscopic, and spectroscopic observations are the net result of the above competing reactions, and are explained as followed.

For $pH < 4.5$ (Fig. 10A), proton-promoted siderite dissolution dominates. Precipitation occurs simultaneously with the redox reaction, resulting in a reduced net dissolution rate as compared to control observations. At circumneutral pH values of 4.5–10 (Fig. 10B), the solubility of Cr–Fe-hydroxide precipitates is at a minimum (Sass and Rai, 1987). Rapid and widespread surface precipitation at both terraces and edge steps inhibits the further dissolution.

For $pH > 10$ (Fig. 10C), the dissolution rate is unusually high as compared to the control condition. As discussed in Section 3.1, the classic model for carbonate minerals dissolution involves parallel protonation and water hydrolysis reactions, which also implies pH-independent dissolution rates for $pH > 6$ (Plummer et al., 1978). Recent surface complexation modeling inputs have suggested the consideration of surface speciation, especially when considering experimental carbonate mineral dissolution rates as a function of $\sum CO_2$ (Schott et al., 2009). The increased dissolution rate of calcite and dolomite in CO_2-free and strongly alkaline solution ($pH > 12$) can be explained by the formation of the negatively charged $>MeO^-$ species at the expense of neutral $>MeOH^0$ species (Pokrovsky and Schott, 2001; Schott et al., 2004, 2009). Interestingly, the redox-sensitive mineral siderite shows the classic pH-independent dissolution behavior in anoxic conditions both in this study and in Duckworth and Martin (2004b) yet has elevated dissolution rate at $pH > 10$ in the presence of oxidants, i.e., chromate in this study and oxygen in Duckworth and Martin (2004b).

Duckworth and Martin (2004b) proposed two possible mechanisms for the elevated dissolution rate in the presence of oxygen: (1) the rapid electron transfer between aqueous $[Fe^{3+}(OH)_4]^-$ and surfacial $>Fe^{II}OH_{(s)}$ groups or (2) the direct attack of surface $>Fe^{II}$ groups by aqueous oxygen. For our study of siderite dissolution in the presence of chromate, an explanation of the elevated dissolution rate in alkaline conditions requires an examination both of the solution and of the surface speciation. Speciation calculation using 40 nM Cr(III), Fe(III) or Fe(II) shows that the predominant Cr(III), Fe(II), and Fe(III) species for $pH > 10$ are $[Cr^{3+}(OH)_4]^-$, $[Fe^{2+}(OH)_3]^-$, and $[Fe^{3+}(OH)_4]^-$, respectively. The observation that rapid dissolution occurs for $pH > 10$ only in the presence of oxidant (i.e., chromate in this study or oxygen in Duckworth and Martin (2004b)) indicates that the oxidation of Fe(II) to Fe(III) and the involvement of these hydroxylated species play important roles. In our case of Cr(VI) as the oxidant, because the redox reaction between Cr(VI) and Fe(II) species only occurs in solution rather than at the mineral surfaces (Eary and Rai, 1989), we therefore consider the second mechanism unlikely in our system. Based on the above information on both solution and surface speciation, we propose that the fast dissolution rate is due to the electron transfer between solution $[Fe^{3+}(OH)_4]^-$ and surfacial $>Fe^{II}OH^0$ or $>Fe^{II}O^-$ groups. In this mechanism, the dissolved $[Fe^{2+}(OH)_3]^-$ is oxidized by CrO_4^{2-} to $[Fe^{3+}(OH)_4]^-$, which then scavenges one electron from the surfacial $>Fe^{II}OH$ or $>Fe^{II}O^-$ groups, causing continued dissolution of siderite. In tandem, the $[Fe^{3+}(OH)_4]^-$ species is reduced to $[Fe^{2+}(OH)_3]^-$, which is re-cycled for further reduction of CrO_{2-}^{4}.

4. CONCLUSIONS AND IMPLICATIONS

The present study combines macroscopic, microscopic, and spectroscopic observations of the siderite surface in the presence of chromate. For all investigated pH conditions, simultaneous dissolution and precipitation occur. Surface precipitation caused by the introduction of Cr(VI) solution appear as round hillocks, which grow into larger sizes after extended reaction time. In addition, regardless of experimental pH, these hillock precipitates are located both at terraces and edge steps with no preferential distribution. These observations are strikingly different from those on siderite or rhodochrosite ($MnCO_3$) surface in the presence of dissolved oxygen as oxidant (Duckworth and Martin, 2004b). The oxidation of siderite by dissolved oxygen under alkaline condition causes the precipitation of hillocks with 10–20 nm height by 100–200 nm diameter, which preferentially form at step sites. In contrast, rhodochrosite surface oxidation by dissolved oxygen results in a continuous growth of layer at neutral pH, as well as precipitation of a patchy layer of hillocks 20–25 nm high by 1–2 μm diameter (Duckworth and Martin, 2004b).

In the presence of Cr(VI) as an oxidant, reactions occur at the siderite surface and involve parallel proton- and water hydrolysis-promoted dissolution, oxidation of dissolved Fe(II) by Cr(VI), and surface precipitation. These reactions occur simultaneously and have different relative importance for varied pH. The dissolution rate for $pH < 4.5$ is slower than that in the control solution. Isolated deep dissolution pits and clustered shallow pits occur simultaneously with surface precipitation. For $5 < pH < 9.5$, the dissolution rate is the slowest, and rapid precipitation is observed at both edge steps and terraces. For $pH > 10$, the dissolution rate is faster than that in the control solution and can be explained by the electron transfer facilitated by $[Fe^{3+}(OH)_4]^-$. Dissolution and re-precipitation of round hillocks are observed. The surface precipitates are identified as low-solubility nano-sized Cr(III)–Fe(III)-hydroxide. These results provide important insights for the more general topic of the interactions between reduced iron in minerals and aqueous-phase inorganic or organic oxidants.

ACKNOWLEDGEMENTS

The authors acknowledge Christopher Letini (SEAS) for providing a synthetic hematite sample and David Lange (CNS) for assistance with XPS data collection. The Center for Nanoscale Systems (CNS) is a member of the National Nanotechnology Infrastructure Network (NNIN), which is supported by the National Science Foundation under NSF award no. ECS-0335765. Comments from the editor and two anonymous reviewers greatly improved the manuscript.

APPENDIX A. SUPPLEMENTARY DATA

Supplementary data associated with this article can be found, in the online version, at doi:10.1016/j.gca.2011.06.024.

REFERENCES

Ahmed K. M., Bhattacharya P., Hasan M. A., Akhter S. H., Alam S. M. M., Bhuyian M. A. H., Imam M. B., Khan A. A. and Sracek O. (2004) Arsenic enrichment in groundwater of the alluvial aquifers in Bangladesh: an overview. *Appl. Geochem.* **19**, 181–200.

Amonette J. E. and Rai D. (1990) Identification of noncrystalline (Fe, Cr)$(OH)_3$ by infrared-spectroscopy. *Clays Clay Miner.* **38**, 129–136.

Aronniemi M., Sainio J. and Lahtinen J. (2005) Chemical state quantification of iron and chromium oxides using XPS: the effect of the background subtraction method. *Surf. Sci.* **578**, 108–123.

Benezeth P., Dandurand J. L. and Harrichoury J. C. (2009) Solubility product of siderite ($FeCO_3$) as a function of temperature (25–250 degrees C). *Chem. Geol.* **265**, 3–12.

Blowes D. W., Ptacek C. J. and Jambor J. L. (1997) In-situ remediation of Cr(VI)-contaminated groundwater using permeable reactive walls: laboratory studies. *Environ. Sci. Technol.* **31**, 3348–3357.

Braun R. D. (1991) Solubility of iron(III) carbonate at temperatures between 30 and 80-degrees. *Talanta* **38**, 205–211.

Coleman M. L., Hedrick D. B., Lovley D. R., White D. C. and Pye K. (1993) Reduction of Fe(III) in sediments by sulfate-reducing bacteria. *Nature* **361**, 436–438.

Duckworth O. W., Cygan R. T. and Martin S. T. (2004) Linear free energy relationships between dissolution rates and molecular modeling energies of rhombohedral carbonates. *Langmuir* **20**, 2938–2946.

Duckworth O. W. and Martin S. T. (2003) Connections between surface complexation and geometric models of mineral dissolution investigated for rhodochrosite. *Geochim. Cosmochim. Acta* **67**, 1787–1801.

Duckworth O. W. and Martin S. T. (2004a) Dissolution rates and pit morphologies of rhombohedral carbonate minerals. *Am. Miner.* **89**, 554–563.

Duckworth O. W. and Martin S. T. (2004b) Role of molecular oxygen in the dissolution of siderite and rhodochrosite. *Geochim. Cosmochim. Acta* **68**, 607–621.

Eary L. E. and Rai D. (1988) Chromate removal from aqueous wastes by reduction with ferrous ion. *Environ. Sci. Technol.* **22**, 972–977.

Eary L. E. and Rai D. (1989) Kinetics of chromate reduction by ferrous-ions derived from hematite and biotite at 25-degrees-C. *Am. J. Sci.* **289**, 180–213.

Erdem M., Gur F. and Tumen F. (2004) Cr(VI) reduction in aqueous solutions by siderite. *J. Hazard. Mater.* **113**, 219–224.

Fendorf S., Eick M. J., Grossl P. and Sparks D. L. (1997) Arsenate and chromate retention mechanisms on goethite.1. Surface structure. *Environ. Sci. Technol.* **31**, 315–320.

Golubev S. V., Benezeth P., Schott J., Dandurand J. L. and Castillo A. (2009) Siderite dissolution kinetics in acidic aqueous solutions from 25 to 100 degrees C and 0 to 50 atm pCO_2. *Chem. Geol.* **265**, 13–19.

Greenberg J. and Tomson M. (1992) Precipitation and dissolution kinetics and equlibria of aqueous ferrous carbonate vs temperature. *Appl. Geochem.* **7**, 185–190.

Hansel C. M., Wielinga B. W. and Fendorf S. R. (2003) Structural and compositional evolution of Cr/Fe solids after indirect chromate reduction by dissimilatory iron-reducing bacteria. *Geochim. Cosmochim. Acta* **67**, 401–412.

Horcas I., Fernandez R., Gomez-Rodriguez J. M., Colchero J., Gomez-Herrero J., and Baro A. M. (2007) WSXM: a software for scanning probe microscopy and a tool for nanotechnology. *Rev. Sci. Instrum.* **78**.

Jensen D. L., Boddum J. K., Tjell J. C. and Christensen T. H. (2002) The solubility of rhodochrosite ($MnCO_3$) and siderite ($FeCO_3$) in anaerobic aquatic environments. *Appl. Geochem.* **17**, 503–511.

Junta Rosso J. L. and Hochella M. F. (1996) The chemistry of hematite {001} surfaces. *Geochim. Cosmochim. Acta* **60**, 305–314.

La Force M. J., Hansel C. M. and Fendorf S. (2002) Seasonal transformations of manganese in a palustrine emergent wetland. *Soil Sci. Soc. Am. J.* **66**, 1377–1389.

Liu C. X., Kota S., Zachara J. M., Fredrickson J. K. and Brinkman C. K. (2001) Kinetic analysis of the bacterial reduction of goethite. *Environ. Sci. Technol.* **35**, 2482–2490.

Lovley D. R. (1991) Dissimilatory Fe(III) and Mn(IV) reduction. *Microbiol. Rev.* **55**, 259–287.

Macinnis I. N. and Brantley S. L. (1992) The role of dislocations and surface-morphology in calcite dissolution. *Geochim. Cosmochim. Acta* **56**, 1113–1126.

Nealson K. H. and Saffarini D. (1994) Iron and manganese in anaerobic respiration–environmental significance, physiology, and regulation. *Annu. Rev. Microbiol.* **48**, 311–343.

Palmer C. D. and Wittbrodt P. R. (1991) Processes affecting the remediation of chromium-contaminated sites. *Environ. Health Perspect.* **92**, 25–40.

Parkhurst D. L. and Appelo C. A. J., 1999. User's Guide to PHREEQC (Version 2) – A computer Program for Speciation, Batch-reaction, One-dimensional Transport, and Inverse Geochemical Calculations. *US Geol. Surv. Water Res. Inv. Rept*. 99-4259.

Patterson R. R., Fendorf S. and Fendorf M. (1997) Reduction of hexavalent chromium by amorphous iron sulfide. *Environ. Sci. Technol.* **31**, 2039–2044.

Plummer L. N., Wigley T. M. L. and Parkhurst D. L. (1978) Kinetcs of calcite dissolution in CO_2-water systems at 5-degree-C to 60-degree-C and 0.0 to 1.0 atm CO_2. *Am. J. Sci.* **278**, 179–216.

Pokrovsky O. S. and Schott J. (2001) Kinetics and mechanism of dolomite dissolution in neutral to alkaline solutions revisited. *Am. J. Sci.* **301**, 597–626.

Pokrovsky O. S. and Schott J. (2002) Surface chemistry and dissolution kinetics of divalent metal carbonates. *Environ. Sci. Technol.* **36**, 426–432.

Sass B. M. and Rai D. (1987) Solubility of amorphous chromium(III)-iron(III) hydroxide solid-solutions. *Inorg. Chem.* **26**, 2228–2232.

Schott J., Pokrovsky O. S. and Golubev S. V. (2004) Surface coordination theory and the dissolution/precipitation rates of carbonate minerals in a wide range of T, pCO(2) and solution composition. *Geochim. Cosmochim. Acta* **68**, A142.

Schott J., Pokrovsky O. S., and Oelkers E. H., 2009. The link between mineral dissolution/precipitation kinetics and solution chemistry. In Thermodynamics and Kinetics of Water-Rock Interaction (eds. E. H. Oelkers and J. Schott), . *Rev. Mineral. Geochem*. Mineralogical Society of America. **70**, 207-258.

Schwertmann U. and Cornell R. M. (2000) *Iron Oxides in the Laboratory: Preparation and Characterization*. Wiley-VCH, Weinheim, Germany.

Schwertmann U., Gasser U. and Sticher H. (1989) Chromium-for-iron substituion in synthetic goethites. *Geochim. Cosmochim. Acta* **53**, 1293–1297.

Shiraki R., Rock P. A. and Casey W. H. (2000) Dissolution kinetics of calcite in 0.1 m NaCl solution at room temperature: an atomic force microscopic (AFM) study. *Aquat. Geochem.* **6**, 87–108.

Silva C. A. R., Liu X. W. and Millero F. J. (2002) Solubility of siderite ($FeCO_3$) in NaCl solutions. *J. Solution Chem.* **31**, 97–108.

Smedley P. L. and Kinniburgh D. G. (2002) A review of the source, behaviour and distribution of arsenic in natural waters. *Appl. Geochem.* **17**, 517–568.

Sosulnikov M. I. and Teterin Y. A. (1992) X-ray photoelectron studies of Ca, Sr and Ba and their oxides and carbonates. *J. Electron Spectrosc. Relat. Phenom.* **59**, 111–126.

Spiccia L. and Casey W. H. (2007) Synthesis of experimental models for molecular inorganicgeochemistry – A review with examples. *Geochim. Cosmochim. Acta* **71**, 5590–5604.

Stel H. (2009) Diagenetic crystallization and oxidation of siderite in red bed (Buntsandstein) sediments from the Central Iberian Chain, Spain. *Sediment. Geol.* **213**, 89–96.

Stipp S. L. and Hochella M. F. (1991) Structure and bonding environments at the calcite surface as observed with X-ray photoelectron-spectroscopy (XPS) and low-energy electron-diffraction (LEED). *Geochim. Cosmochim. Acta* **55**, 1723–1736.

Tang Y., Michel F. M. L. Z., Harrington R., Parise J. B. and Reeder R. J. (2010) Structural properties of the Cr(III)–Fe(III)-oxyhydroxide series. *Chem. Mater.* **3589**, 3598.

Testemale D., Dufaud F., Martinez I., Benezeth P., Hazemann J. L., Schott J. and Guyot F. (2009) An X-ray absorption study of the dissolution of siderite at 300 bar between 50 degrees C and 100 degrees C. *Chem. Geol.* **259**, 8–16.

Vajpei A. C., Rousset A., Uma Chandra. K., Saraswat I. P. and Mathur V. K. (1989) The characterization and thermal transformations of coprecipitated iron(III)-chromium(III)-hydroxide systems. *Solid State Ionics* **32–3**, 741–748.

Van Cappellen P., Charlet L., Stumm W. and Wersin P. (1993) A surface complexation model of the carbonate mineral-aqueous solution interface. *Geochim. Cosmochim. Acta* **57**, 3505–3518.

Wielinga B., Mizuba M. M., Hansel C. M. and Fendorf S. (2001) Iron promoted reduction of chromate by dissimilatory iron-deducing bacteria. *Environ. Sci. Technol.* **35**, 522–527.

Zachara J. M., Ainsworth C. C., Brown G. E., Catalano J. G., McKinley J. P., Qafoku O., Smith S. C., Szecsody J. E., Traina S. J. and Warner J. A. (2004) Chromium speciation and mobility in a high level nuclear waste vadose zone plume. *Geochim. Cosmochim. Acta* **68**, 13–30.

Zachara J. M., Fredrickson J. K., Li S. M., Kennedy D. W., Smith S. C. and Gassman P. L. (1998) Bacterial reduction of crystalline Fe^{3+} oxides in single phase suspensions and subsurface materials. *Am. Miner.* **83**, 1426–1443.

Associate editor: Jacques Schott